First measurement of ^{30}S + α resonant elastic scattering for the ^{30}S(α, p) reaction rate

D. Kahl,[1,2,*] H. Yamaguchi (山口英斉),[1] S. Kubono (久保野茂),[1,3,4] A. A. Chen,[5] A. Parikh,[6] D. N. Binh,[1,†] J. Chen (陈俊),[5,‡]
S. Cherubini,[7,8] N. N. Duy,[9,10,§] T. Hashimoto (橋本尚志),[1,‖] S. Hayakawa (早川勢也),[1] N. Iwasa (岩佐直仁),[11]
H. S. Jung (정효순),[12] S. Kato (加藤静吾),[13] Y. K. Kwon (권영관),[12,‖] S. Nishimura (西村俊二),[3] S. Ota (大田晋輔),[1]
K. Setoodehnia,[5,¶] T. Teranishi (寺西高),[14] H. Tokieda (時枝紘史),[1] T. Yamada (山田拓),[11,#]
C. C. Yun (윤종철),[12,‖] and L. Y. Zhang (张立勇)[4,**]

[1]*Center for Nuclear Study (CNS), the University of Tokyo, RIKEN campus, 2-1 Hirosawa, Wako, Saitama 351-0198, Japan*
[2]*School of Physics & Astronomy, the University of Edinburgh, James Clerk Maxwell Building, Peter Guthrie Tait Road,
Edinburgh EH9 3FD, United Kingdom*
[3]*RIKEN Nishina Center, 2-1 Hirosawa, Wako, Saitama 351-0198, Japan*
[4]*Institute of Modern Physics, Chinese Academy of Science, Nanchang Road 509, Lanzhou 730000, People's Republic of China*
[5]*Department of Physics & Astronomy, McMaster University, 1280 Main St West, Hamilton, Ontario L8S 4M1, Canada*
[6]*Departament de Física, Universitat Politècnica de Catalunya, c/Comte d'Urgell 187, Barcelona 08036, Spain*
[7]*Laboratori Nazionali del Sud-INFN, Catania 95123, Italy*
[8]*Dipartimento di Fisica e Astronomia, Università di Catania, Catania 95123, Italy*
[9]*Department of Physics, Dong Nai University, 4 Le Quy Don, Tan Hiep Ward, Bien Hoa City, Dong Nai, Vietnam*
[10]*Institute of Physics, Vietnam Academy of Science and Technology, 10 Dao Tan, Ba Dihn, Hanoi, Vietnam*
[11]*Department of Physics, Tohoku University, Aoba, Sendai, Miyagi 980-8578, Japan*
[12]*Department of Physics, Chung-Ang University, Seoul 156-756, Republic of Korea*
[13]*Department of Physics, Yamagata University, 1-4-12 Kojirakawa-machi, Yamagata 990-8560, Japan*
[14]*Department of Physics, Kyushu University, 744 Motooka, Nishi-ku, Fukuoka 819-0395, Japan*

Background: Type I x-ray bursts are the most frequently observed thermonuclear explosions in the galaxy, resulting from thermonuclear runaway on the surface of an accreting neutron star. The ^{30}S(α, p) reaction plays a critical role in burst models, yet insufficient experimental information is available to calculate a reliable, precise rate for this reaction.

Purpose: Our measurement was conducted to search for states in ^{34}Ar and determine their quantum properties. In particular, natural-parity states with large α-decay partial widths should dominate the stellar reaction rate.

Method: We performed the first measurement of ^{30}S + α resonant elastic scattering up to a center-of-mass energy of 5.5 MeV using a radioactive ion beam. The experiment utilized a thick gaseous active target system and silicon detector array in inverse kinematics.

Results: We obtained an excitation function for ^{30}S(α, α) near 150° in the center-of-mass frame. The experimental data were analyzed with R-matrix calculations, and we observed three new resonant patterns between 11.1 and 12.1 MeV, extracting their properties of resonance energy, widths, spin, and parity.

Conclusions: We calculated the resonant thermonuclear reaction rate of ^{30}S(α, p) based on all available experimental data of ^{34}Ar and found an upper limit about one order of magnitude larger than a rate determined using a statistical model. The astrophysical impact of these two rates has been investigated through one-zone postprocessing type I x-ray burst calculations. We find that our new upper limit for the ^{30}S(α, p)^{33}Cl rate significantly affects the predicted nuclear energy generation rate during the burst.

---

*daid.kahl@ed.ac.uk

†Present address: 30 MeV Cyclotron Center, Tran Hung Dao Hospital, Hoan Kiem District, Hanoi, Vietnam.

‡Present address: Nuclear Data Center, National Superconducting Cyclotron Laboratory, Michigan State University, 640 S. Shaw Ln, East Lansing, Michigan 48824, USA.

§Present address: Department of Physics, Sungkyunkwan University, 300 Chunchun-dong, Jangan-ku, Suwon 400-746, Republic of Korea.

‖Present address: Institute for Basic Science, Daejeon 305-811, Korea.

I. INTRODUCTION

Type I x-ray bursters (XRBs) are a class of astronomical objects observed to increase in luminosity by factors of typically

¶Present address: Department of Physics, North Carolina State University, 2401 Stinson Dr, Raleigh, NC 27607, USA.

#Present address: Yokohama Semiconductor Co., Ltd, Japan.

**Present address: Key Laboratory of Optical Astronomy, National Astronomical Observatories, Chinese Academy of Sciences, Beijing 100012, China.

tens to several hundreds [1] for a short period of time (tens of seconds) with the photon flux peaking in the x ray and a total energy output of about $10^{39} - 10^{40}$ ergs [2,3]. The sources of such emissions repeat these outbursts typically on time scales of hours to days, allowing for the extensive study of the burst morphology of individual XRBs. In our galaxy, over ninety such sources are presently known since their initial discovery some forty years ago. XRBs are modelled very successfully as a neutron star accreting material rich in hydrogen and/or helium from a low-mass companion. The accretion mechanism causes the formation of an electron-degenerate envelope around the neutron star, where the thin-shell instability triggers a runaway thermonuclear explosion at peak temperatures of 1.3–2.0 GK [4–8], which we observe as an x-ray burst.

The sharp rise of the x-ray fluence is understood to be powered by explosive helium burning on the neutron-deficient side of the Segrè chart [6,8–11]. In a mixed hydrogen and helium shell, the explosive nucleosynthesis initially manifests as a series of $(\alpha,p)(p,\gamma)$ reactions on oxygen seed nuclei near the proton drip line (^{14,15}O), called the αp process [12]. One such sequence in this burning pathway is

$$3\alpha \rightarrow {}^{12}\text{C}(p,\gamma){}^{13}\text{N}(p,\gamma){}^{14}\text{O}(\alpha,p){}^{17}\text{F}(p,\gamma)$$
$${}^{18}\text{Ne}(\alpha,p){}^{21}\text{Na}(p,\gamma){}^{22}\text{Mg}(\alpha,p){}^{25}\text{Al}, \quad (1)$$

which continues as

$$\,^{25}\text{Al}(p,\gamma){}^{26}\text{Si}(\alpha,p){}^{29}\text{P}(p,\gamma)\mathbf{{}^{30}S(\alpha,p)}\mathbf{{}^{33}Cl}(p,\gamma)$$
$${}^{34}\text{Ar}(\alpha,p){}^{37}\text{K}(p,\gamma){}^{38}\text{Ca}(\alpha,p){}^{41}\text{Sc}. \quad (2)$$
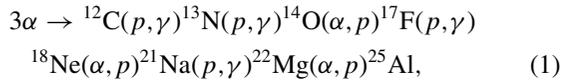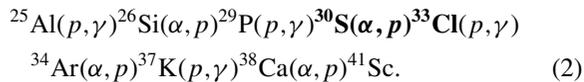
In this sequence, the (α,p) reactions proceed through $T_z = \frac{N-Z}{2} = -1$ compound nuclei. The αp process gives way to the rapid proton-capture process (rp process) near the $Z \approx 20$ region owing to the ever increasing Coulomb barrier and decreasing (α,p) Q values. Aside from the two protons consumed in the nuclear trajectory from ^{12}C to ^{14}O, the αp process is schematically pure helium burning (since the abundance of hydrogen is constant), and it does not include any β^+ decays which tend to hamper the energy generation rate in explosive nucleosynthesis.

While a plethora of nuclear processes tend to take place in a given regime of stellar nucleosynthesis, typically the precise rates of only a handful of these processes influence the predicted nature and magnitude of actual astrophysical observables. It is these specific nuclear quantities which should be well constrained by laboratory experimentation. This general picture is confirmed in XRBs, where the nuclear reaction network includes hundreds of species and thousands of nuclear transmutations. Studies have shown that it is only a small subset of these nuclear transmutations which need to be known precisely, as they make a predominant contribution to the nuclear trajectory to higher mass and energy generation [13], at least for the examined models.

The ^{30}S(α,p) reaction is identified as one such important reaction, contributing more than 5% to the total energy generation [13], influencing the elemental abundances in the burst ashes [13] relevant to compositional inertia (see, e.g., [14] for a description of this phenomenon), moving material away from the ^{30}S waiting point [15], and possibly accounting for double peaked XRBs [16]. A recent study found the ^{30}S(α,p) reaction sensitivity in XRBs among the top four in a single zone model

[17], as well as having a prominent (but unquantified) impact on the burst light curve in a multizone model.

A firmer understanding of the input nuclear physics for XRB models will allow for more reliable comparison with observations to constrain neutron star binary system properties, such as accretion rate and metallicity, as well as the neutron star radius itself [18–23].

The (α,p) reactions occurring on lower mass nuclei such as ^{14}O and ^{18}Ne have been measured directly [24–28], and the properties of resonances in the compound nuclei ^{18}Ne and ^{22}Mg have been the subject of a number of indirect studies (see, e.g., Refs. [29,30] and references therein). In spite of these extensive works, those cross sections still remain quite uncertain. Unfortunately, the situation is much more dire in the case of the (α,p) reactions induced on higher mass targets such as ^{30}S. The only experimental information on the structure of ^{34}Ar above the α threshold and the ^{30}S(α,p) stellar reaction rate is limited to a preliminary report on a transfer reaction study of the compound nucleus ^{34}Ar at high excitation energy [31] and a time-reversal study [32]. The present work is the first experimental investigation using the entrance channel ^{30}S $+ \alpha$.

II. EXPERIMENT

We performed the first measurement of α resonant elastic scattering on a ^{30}S radioactive isotope beam (RIB) using a thick target in inverse kinematics [33]. The experiment was carried out at the CNS Radioactive Ion Beam separator (CRIB) [34,35], owned and operated by the Center for Nuclear Study (CNS), the University of Tokyo, and located in the RIKEN Nishina Center. The CRIB facility has been a workhorse for measurements of elastic scattering of primarily astrophysical interest [36–49], schematically using similar techniques to the one adopted in the present study.

The ^{30}S RIB was produced in flight using the ^{3}He(^{28}Si,^{30}S)n transfer reaction. A ^{28}Si^{9+} primary beam was extracted from an electron cyclotron resonance ion source and accelerated to 7.3 MeV/u by the RIKEN AVF cyclotron ($K \approx 70$) with a typical intensity of 80 pnA. We impinged the ^{28}Si beam on the production target located at the entrance focal plane to CRIB, comprised of a windowed, cryogenic gas cell [50]. ^{3}He gas at 400 Torr was cooled to an effective temperature of 90 K with LN$_2$; the gas was confined by 2.5-μm Havar windows in a cylindrical chamber with a length of 80 mm and a diameter of 20 mm, yielding a ^{3}He target thickness of approximately 1.7 mg cm^{-2}. As the fully stripped species ^{30}S^{16+} is the easiest to separate and distinguish from the primary beam, we used Be (2.5 μm) and C (300 μg cm^{-2}) stripper foils immediately after the production target; when the Be (C) stripper foil was new, the ^{30}S^{16+} purity was 88% (67%), but decreased dramatically within hours as the beam degraded the foils. Studies are ongoing to investigate the effects of stripper foil degradation on beam purity and intensity. The resulting cocktail beam was separated by a double achromatic system (set to $\frac{\Delta p}{p} = 1.875\%$ with slits at the dispersive focal plane) and further purified with a Wien (velocity) filter. The ^{30}S RI beam arrived on target with typical purity of 28% and an intensity of 8×10^3 pps, successfully injecting 1.6×10^9 ^{30}S ions during the main measurement over two days.
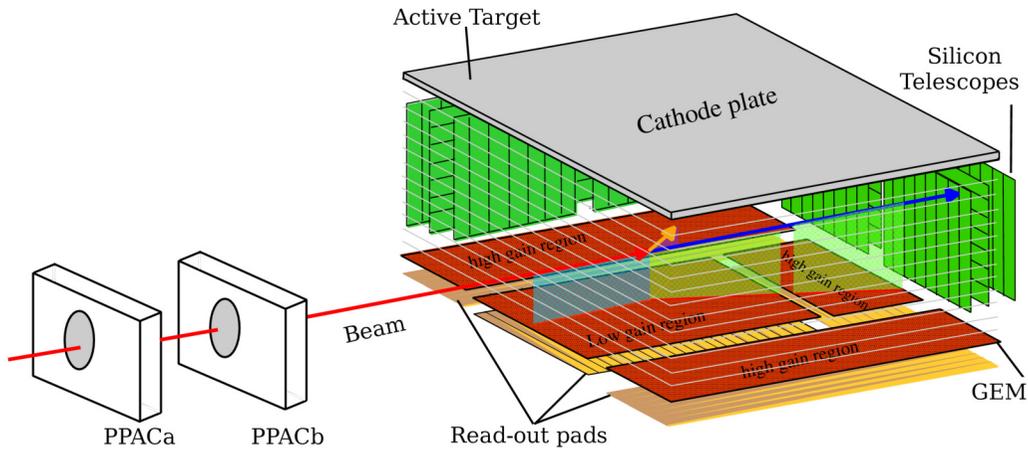
FIG. 1. Schematic of the experimental setup, consisting of two parallel plate avalanche counters (PPACs), the active target, and silicon telescope arrays. Note that between PPACb and the active target, the beam impinges on an entrance window, which retains the active target fill gas. The beam is tracked in the central low-gain region ("active target region," 20 cm), surrounded on three sides by high-gain regions and silicon telescopes to measure outgoing light ions (right side telescope not depicted). Beneath each gas electron multiplier (GEM) is a readout pattern, separated into 4 mm thick backgammon pads. ΔE is simply proportional to the charge collected by each pad. The coordinate system is one where the beam axis defines positive Z, the rest following left-handed conventions. Z and X positions are determined by the pad number and comparing charge collection on either side of the backgammon, respectively. The Y position is determined by the electron drift time.

The setup at the experimental focal plane, shown in Figs. 1 and 2, consisted of two beamline monitors, an active target system (see below), and an array of silicon strip detectors (SSDs). The beamline monitors were parallel plate avalanche counters (PPACs, enumerated "a" and "b," respectively) [51], which served to track the beam ions event by event and to produce the trigger signal for the data acquisition system (DAQ). The DAQ triggered when both PPACs fired in coincidence with an SSD to obtain the physics of interest; the DAQ also triggered in a downscaled mode for $\frac{1}{n}$ PPAC coincidences ($n = 2.2 \times 10^4$) regardless of the SSD signals. This trigger setup is standard in CRIB experiments, and it allows for event-by-event analysis of scattering events as well as simultaneous diagnosis of the RIB for systematic behavior while keeping a total trigger rate <1 kHz. Due to a DAQ error, we could only fully analyze the data from the forward right-side SSD.

During the RIB production, the efficiency of each PPAC was determined to be quite high (>99%) considering the number
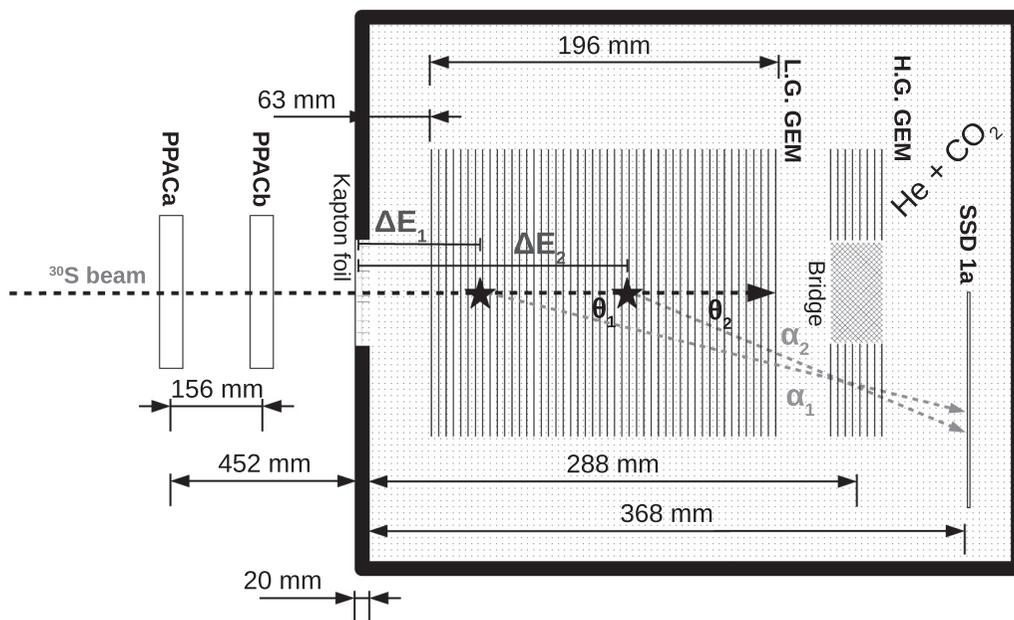
FIG. 2. Top-down cartoon of the experimental setup and the detectors used in the data analysis (not to scale—PPACs in particular are much further from the active target chamber than depicted). The differences between a higher energy scattering (denoted "α_1") and a lower energy scattering ("α_2") are shown.

of events recorded by each detector; however, at the start of the scattering measurement PPACb was damaged by several discharges, and its efficiency became somewhat lower ($\sim$90%) for most of the experiment. Each SSD was 0.5 mm thick and had an active area of 91×91 mm^2, eight strips on one side, and a single pad on the reverse. A scattering chamber filled with about $\frac{1}{4}$ atm 90% ^{nat}He + 10% CO$_2$ gas mixture housed both the active target system and the SSDs.[1] The He + CO$_2$ gas pressure was monitored continuously throughout the scattering measurement and managed by a dedicated system; we set the gas flow controller to circulate fresh gas into the chamber at 20 standard liters per minute with the evacuation rate regulated to keep a constant gas pressure of 194.2 ± 0.5 Torr during the entire measurement. The gas-filled chamber was sealed off from the beamline vacuum with a 7.4-μm Kapton foil; the entrance window was 40 mm in diameter.

An active target is a device where a material serves simultaneously as a target and part of a detector, in principle allowing one to perform direct measurements at a beam interaction position. The readout section of our active target is an etched copper plate placed under the field cage, opposite to the cathode top plate, so that electrons created in the electric field of the cage by ionizing radiation drift towards it. The readout pads are separated into four sections: one for detecting the beam or heavy recoils and three for detecting outgoing light ions. Forty-eight pads comprise the beam readout section, while the regions for detecting light ions are comprised of eight rectangular pads each. The pads are 3.5 mm in depth, surrounded by 0.25 mm of insulation on all sides (making 0.5 mm of insulation between each pad). Each pad is also bisected diagonally into two congruent right triangles, so that the collected charge can be read out from two opposing sides (backgammon pads). The section for detecting the beam ions is the largest and located at the center, slightly shifted towards the beam upstream direction after installation in the scattering chamber. The regions for detecting light ions surround the beam section on the left, right, and downstream sides. Gas electron multiplier (GEM) foils were used to set different effective gains over the beam and light-ion regions. Over the center of the downstream high-gain GEMs was a bridge to prevent the unscattered beam ions from saturating the light ion signals.

We quantified the measurement capabilities of the active target using both online and offline measurements. For the low-gain region, we compared the position of ^{30}S ions derived from the active target to those determined by extrapolation of the PPAC data. For the high-gain region, we analyzed the aggregate track width of radiation emitted from a standard α source in a fixed position as measured by the active target; the tracks were software gated to be in coincidence with a geometrically central SSD strip. By assuming a standard CRIB PPAC resolution of $\sim$1 mm based on our experience and the known finite strip size of the SSD, we varied the active target resolution in a Monte Carlo simulation until the calculations agreed with the data. The performance of the active target depended on the type of measurement, quoted below at 1σ. The Y position, determined by the electron drift time, was the most precise being $\leqslant$0.5 mm;
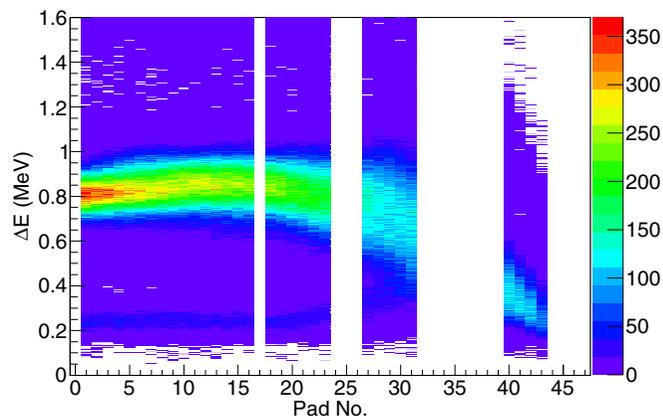
FIG. 3. Calibrated Bragg curve of the unscattered ^{30}S beam over the low-gain region of the active target. The depth of each pad is 4 mm with the beam penetration depth correlated with the pad number. Data from several pads are not shown for a variety of reasons; in general it was either because the electronics did not record a signal, or the energy deposit was arbitrarily lower than expected.

the high precision of the drift-time measurement enabled us to confirm the PPAC resolution, which was found to be 0.9 mm. The X-position resolution, determined by charge division in the backgammon pads, was 3 mm.

In the present work, the typical ^{30}S scattering laboratory angle and change in energy loss was difficult to reliably distinguish from the unscattered beam given the above resolution for the low-gain GEM in X.

Considering the close spacing of the high-gain GEM data and their relatively large distance from typical scattering locations, extrapolating the vector of an α particle's track results in a large uncertainty. Instead, we found that averaging the pad X and Y data over the center (in Z) of the high-gain GEM reduced the uncertainty and was sufficient for our purposes.

The ^{30}S energy on target was measured to be 48.4 ± 2.0 MeV. The stopping power for ^{30}S in the He + CO$_2$ gas mixture was determined by both a direct measurement of the beam energy at five target pressures and by a comparison of the shape of the Bragg curve and stopping position of the unscattered ions in the active target as shown in Fig. 3. Excellent agreement was found between the measurements and the prediction using Ziegler's method; the maximum difference between the measured and calculated ^{30}S residual energy was 700 keV or less than 4%. The energy loss and the Bragg curve of the contaminant ^{29}P were also reproduced using an identical approach, giving us confidence in our treatment of the energy loss in the PPACs, entrance window, and He + CO$_2$ gas mixture. The event-by-event particle identification of the cocktail beam is shown in Fig. 4.

We confirmed the energy loss of α particles using a standard triple α source and an α beam created by CRIB, checking that both their Bragg curves and residual energies agreed with the calculations. A calibrated ΔE-E spectrum from the ^{30}S + α scattering measurement is shown in Fig. 5; the figure shows clearly that the measured locus is consistent with the theoretical trend for α particles. The dynamic range of the high-gain GEMs was optimized to be 10–100 keV corresponding to the energy
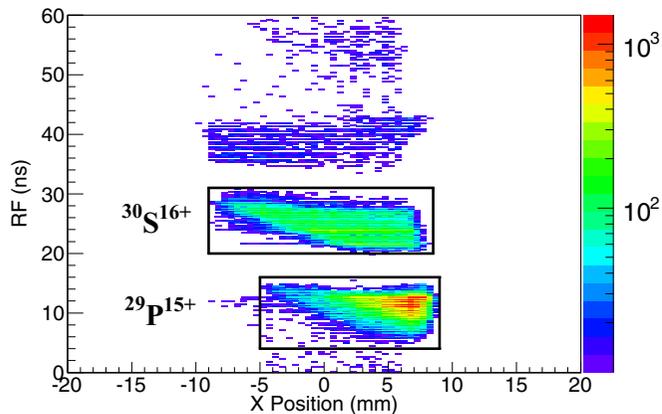
FIG. 4. Timing from rf vs PPACa X position for the unscattered beam, showing gates for ^{30}S and ^{29}P. The rf signal is recorded with PPACa as the start and the cyclotron radio-frequency signal as the stop, and thus it represents a relative flight time between ions in the cocktail beam.

deposit of α particles, which would always be stopped in the first SSD layer unlike high energy protons. As protons with enough energy to reach an SSD deposit <5 keV per pad, they could not be detected by the active target system.

III. ANALYSIS

A. Determination of cross section

We measured (1) the residual energy of α particles using an SSD, (2) the beam trajectory using the two PPACs, and (3) the recoiling α particle position using the high-gain portion of the active target. These three pieces of information are sufficient to determine the center-of-mass energy $E_{c.m.}$ for elastic scattering, defined as

$$E_{c.m.} = \frac{M+m}{4M \cos^2 \vartheta_{lab}} E_\alpha,\qquad(3)$$
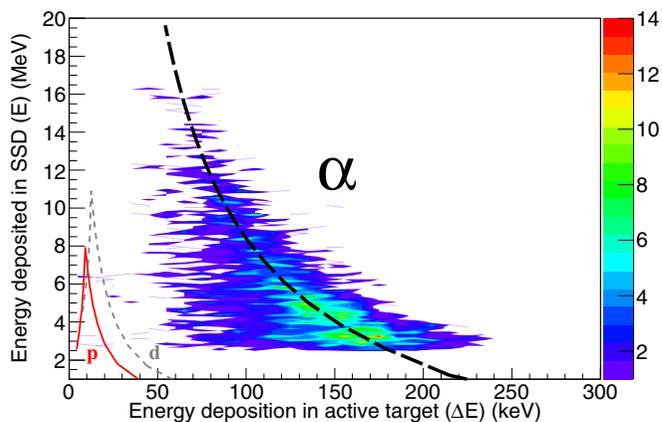
FIG. 5. $\Delta E - E$ plot for light ion particle identification during the ^{30}S + α scattering measurement. The long-dashed black line, short-dashed grey line, and solid (red) line show calculations for α particles, deuterons, and protons, respectively, using the experimental conditions.
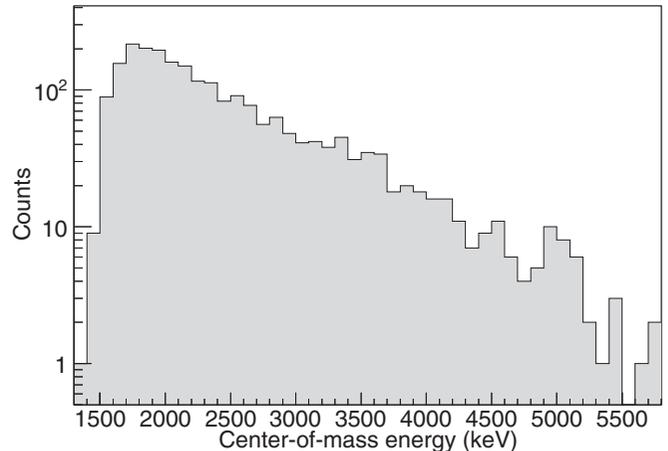
FIG. 6. Energy spectrum of scattered α particles gating on the ^{30}S RIB determined by the kinematic solution. As the high-gain GEM and SSD must both be hit for an event to register, it is only a portion of the total events which are analyzed. Hints of some resonant structure can be seen around 4500 and 5000 keV. The data cut off at low energy as the scattered α particles do not have enough energy to reach the SSD and are instead stopped in the gas.

where M and m are the masses of ^{30}S and ^{4}He, respectively, ϑ_{lab} is the laboratory scattering angle, and E_α is the laboratory energy of the scattered α particle. Using the experimentally verified stopping power of the He + CO_2 gas for ^{30}S ions and α particles, we numerically solved the above kinematic equation event by event. We selected test points along the extrapolated ^{30}S ion trajectory in 1 mm steps, calculating $E_{c.m.}$ according to the beam's energy loss up to each point. Each tested scattering depth fixes the value of ϑ_{lab} by the geometric measurements of the PPACs and high-gain GEM. Finally, the initial α energy was determined with Eq. (3) and its residual energy was calculated considering its energy loss along said path, which we then compared with the energy recorded by the SSD. The algorithm continued until the ^{30}S ion came to rest with no solution being found or when the calculated and measured residual α particle energy disagreed by less than 100 keV, which we define as a true scattering event at that $E_{c.m.}$. In the case that more than one test point satisfied these conditions, we select the $E_{c.m.}$ with the smallest disagreement between the measured and calculated residual α energy. The resulting α spectrum is shown in Fig. 6.

The differential cross section was then calculated using

$$\frac{d\sigma}{d\Omega} = \frac{Y_\alpha S(E_b)}{I_b n \Delta E \Delta\Omega_{c.m.}} \frac{m}{M+m},\qquad(4)$$

where Y_α is the yield of α particles at each energy bin, $S(E_b)$ is the stopping power of ^{30}S in He + CO_2, I_b is the number of ^{30}S beam ions injected into the target, n is the number density of ^{4}He atoms, ΔE is the energy bin size (100 keV), and $\Delta\Omega_{c.m.}$ is the center-of-mass solid angle at each energy bin. The number of beam ions injected into the target I_b was defined as the coincidence between the two PPACs, recorded as a scaler during the run, multiplied by the average ^{30}S purity, which includes a cut for the active target entrance window for successful injection into the target. The lower efficiency of PPACb cancels out in the deduction of the cross section

because we demanded beam particle detection with the PPACs for counting both the number of scattering events and injected beam ions. Since the scattering could take place over a range of target depths, we calculated the solid angle $\Omega_{\text{c.m.}}$ from the vantage point of each actual scattering event and fit the trend with an empirical function. The yield of α particles Y_α was scaled universally by a factor of 2.0 ± 0.1 to match the calculated magnitude of Rutherford scattering at lower energies; a similar deficiency was observed in the number of α particles (produced in the cocktail beam by CRIB) detected by the high-gain GEM compared to the SSD in a low-statistics test run giving a scaling factor 1.8 ± 0.3 (see Secs. II B and III D below and Ref. [52] for further details). A series of measurements are already planned to further investigate and constrain this scaling factor. The resulting excitation function is shown in Fig. 9(a).

B. Sources of background

Detected α particles might originate from a source other than elastic scattering of ^{30}S with the helium nuclei in the target gas. We applied software gates to the PPAC data event by event to ensure the incident beam ions were consistent with the properties of ^{30}S, which removed contributions to the α spectrum induced by other heavy ion species within the cocktail beam.

One might imagine various reactions with the PPACs, Kapton window (stoichiometry $C_{22}H_{10}N_2O_5$), or the CO_2 used as a quenching gas in the active target. The standard PPACs used at CRIB are each filled with 9 Torr C_3F_8 over a length of ≈ 35 mm (≈ 0.3 mg cm^{-2}) confined with 2-μm aluminized Mylar windows ($H_8C_{10}O_4$) and interspaced with a further three 1.5-μm similar foils (8.5 μm in total).

The ^{30}S beam profile on PPACa does not have a line of sight to the high-gain GEM owing to the active target entrance window combined with the bridge over the downstream high-gain GEM, although the edge of the ^{30}S profile on PPACb does have such a line of sight. Thus, we can geometrically rule out PPACa (but not PPACb) as a source of background α particles.

Although the CNO-group elements require some consideration, we can immediately rule out hydrogen as a background source of α particles, because the ^{30}S(p,α) reaction Q value is -8.47 MeV, and the ^{30}S $+ p$ system $E_{\text{c.m.}} < 4$ MeV anywhere after the dispersive focal plane.

As for the entrance window and quenching gas, the Coulomb barriers for ^{30}S $+ ^{12}$C, ^{30}S $+ ^{14}$N, and ^{30}S $+ ^{16}$O are 24.4, 28.0, and 31.3 MeV, respectively. The ^{30}S beam energy impinging on the Kapton window is about 2.34 MeV/u, yielding $E_{\text{c.m.}} = 20.0, 22.3, 24.3$ MeV for nuclear interactions with ^{12}C, ^{14}N, and ^{16}O, respectively. As for the incident ^{30}S beam energy impinging on the He + CO_2 gas, it is about 1.62 MeV/u, which yields $E_{\text{c.m.}} = 13.9, 16.9$ MeV for nuclear interactions with ^{12}C and ^{16}O, respectively. Considering that the center-of-mass energies are always below the respective Coulomb barriers for the entrance window and quenching gas, this implies that the heavy-ion fusion cross sections should be many orders of magnitude lower than that of α elastic scattering.

Although we are not aware of any experimental data concerning ^{30}S-induced heavy-ion reactions, the fusion study with ^{12}C and ^{16}O on the stable isotopes ^{28,29,30}Si by Jordan *et al.* [53] is analogous if we accept isospin symmetry. Their center-of-mass energies broadly overlap with ours sufficiently to make a germane comparison. In that work, the authors see smooth behavior of the excitation functions except in the case of ^{12}C $+ ^{28}$Si, where they report oscillatory behavior between 21 and 26 MeV in ^{12}C bombarding energies, which would correspond to maximum E_α in the range of 5.5–7 MeV from the ^{28}Si$(^{12}$C, ^{4}He) reaction. E_α corresponding to the lowest region of interest in our study of ^{30}S $+ \alpha$ is around 15 MeV ($E_{\text{c.m.}} \approx 4$ MeV). Thus, the only structure seen by Jordan *et al.* is quite far away from the structure we report here.

As relevant to the present study, Jordan *et al.* importantly find smooth cross sections for ^{12}C and ^{16}O with ^{30}Si, the mirror nucleus of ^{30}S. Such behavior implies that a background source of α particles in the present work induced by CNO-group elements should have a relatively flat energy distribution. Figure 9(a) shows that our observed resonant structure is manifested as destructive interference with pure Rutherford scattering. It means that any unaccounted for background of α particles arising from the ^{30}S beam interacting with CNO-group elements would tend to decrease our observed resonance dips and thus our deduced partial widths Γ_i could be modestly smaller than the true values. If we consider the relative differences in the maximum (≈ 60 mb/sr) and minimum (≈ 5 mb/sr) differential cross sections around 5 MeV center-of-mass energy, then a smooth background cannot comprise more than 8% of the measurement in the region of interest. This uncertainty turns out to be smaller than the statistical error and as such can be reasonably neglected.

The main sources of energy-dependent background could be α particles originating from the RIB production target satisfying the $B\rho$ selection as well as contributions from inelastic scattering. The bumps seen in the excitation function around 3.5 MeV in Fig. 9(a) correspond to the region where α particles magnetically selected by CRIB are expected to appear. These background ions are observed clearly in the spectrum of the SSD residual energy against the system time of flight (ToF) in Fig. 7. The ToF is the time between PPACa and the SSD, following Ref. [54]. The figure shows all SSD events gated on incoming ^{30}S ions, about $\approx 80\%$ of which are discarded by the requirements of the kinematic solution. The true elastic scattering events fall within a small locus on the histogram with a specific ToF, depicted by a narrow gate. Conversely, the beamlike α particles span the entire ToF range with temporal spacing exactly corresponding to the inverse of the cyclotron radio-frequency signal, because these ions do not deposit enough energy to trigger the PPAC and merely arrive at the SSD in chance coincidence with a ^{30}S ion at the PPAC. Ordinarily, the relation of the PPAC signal and cyclotron radio frequency corresponds to a relative flight time of a beam ion within the cocktail beam (see Fig. 4), but this relation does not hold for such a chance coincidence. Although most of such events are easily discarded, there is a small region of overlap where the beamlike α particles may contribute as much as 20% of the data in this region.
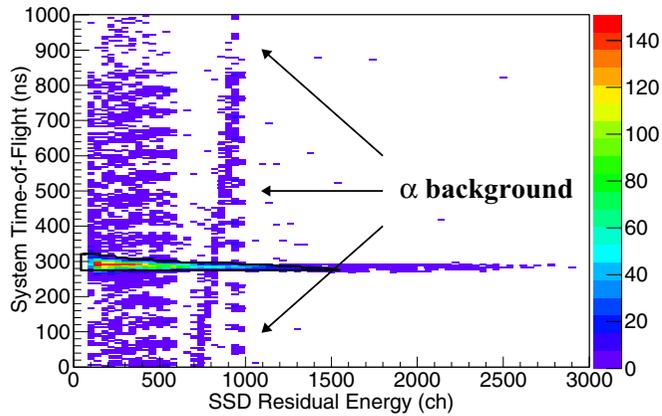
FIG. 7. Residual light ion energy as measured by the SSD in channels on the abscissa against the system ToF in nanoseconds on the ordinate. Significant α background is seen around channel 1000 in the SSD energy. The locus of true elastic scattering events selected by the kinematic solution fall within the depicted gate; however, it can be observed that one locus of the beamlike α particles overlaps with the region of the true events. See the text.

There is another particle group to the left of the α background in Fig. 7 which is quite unusual, as its residual energy is positively correlated with its system flight time. The nature of this locus is not certain but is most likely associated with light ejecta resulting from heavy ions striking the Wien filter electrodes in chance coincidence with a ^{30}S beam ion. Considering the number of events in this locus per ns, we estimate it may contribute 5% of the data in Fig. 9(a) near 3.3 MeV.

As described below in Sec. III D, introducing individual resonances in this region with widths equal to the theoretical limit made no discernible change to the calculated excitation function given our energy resolution. Changing the fill-gas to perform background measurements with an active target necessitates adjusting the GEM high voltage settings (which would still not guarantee identical operating conditions) as well as replication of all tuning and calibration measurements, which requires a significantly larger investment of time compared to changing the target gas in an ordinary target. Although we prepared to make such a measurement with an Ar + CO$_2$ gas mixture (as in our previous measurements, e.g., [46]), unfortunately we did not have enough time. Using the Wien filter to steer the beam, we determined that a vast majority of the beamlike α particles are confined to a narrow energy region.

Further analysis of Fig. 7 also sheds some light on the origin of the scaling factor of 2 applied to obtain the correct magnitude of the absolute value of the elastic scattering differential cross section. As stated above, about 20% of the events fall within a narrow locus and are consistent with bona fide elastic scattering events according to the kinematic solution algorithm. More than three times this many events (∼60% of the entire spectrum) fall within the depicted gate, but over 70% of the events within this gate have no corresponding high-gain GEM data (>40% of the entire spectrum), thus ϑ_{lab} is unknown and Eq. (3) cannot be solved. The solid angle of the right side of

the downstream high-gain GEM is about 50% that of the SSD, and the Rutherford cross section is known to go as $(\sin^4 \frac{\theta}{2})^{-1}$, indicating it does not change appreciably over a small change ($\approx 10°$) in ϑ_{lab}. This implies that about $\frac{1}{2}$ of the events in the ToF-E locus of Fig. 7 should be in coincidence with the high-gain GEM, but only about $\frac{1}{4}$ actually have high-gain GEM data. These results are quite consistent with our scaling factor of 2.

As for possible contributions from inelastic scattering, the first excited state of ^{30}S is relatively high at $E_{\text{1x}} =$ 2.21 MeV and with a spin parity of 2^+. The increased scattering threshold as well as the requirement for $\ell \geqslant 2$ from the angular momentum selection rules indicates that the widths, which decrease with increasing ℓ, suggest a significantly lower cross section than elastic scattering. For example, in other studies of α elastic scattering, this contribution was found to be less than 10% [43,46], where the first excited states are much lower in energy. Moreover, as the resonances we analyzed were in the region of $4.0 \leqslant E_{\text{c.m.}} \leqslant 5.6$ MeV, contributions from inelastic scattering would show up near $1.8 \leqslant E_{\text{c.m.}} \leqslant 3.4$ MeV in the elastic spectrum, where resonances were neither resolved nor analyzed in our data. Therefore, it is reasonable to neglect any possible contribution from inelastic scattering in the present analysis; thus, we assume the total width can be expressed as $\Gamma = \Gamma_{\alpha_0} + \Gamma_p$.

C. Experimental error

A number of different factors can influence the determination of the center-of-mass energy $E_{\text{c.m.}}$ for a given event: the spread in the beam energy from the momentum selection as well as straggling, the SSD resolution for measurement of the α particle residual energy, the straggling of the α particle, and the position determinations of both the recoiling α and beam ion. However, since we use the geometric measurements to determine ϑ_{lab} and the residual energy of the outgoing α particle to deduce E_α, these have the most profound effect on the determination of $E_{\text{c.m.}}$. Based on Eq. (3), the uncertainty in the center-of-mass energy $\Delta E_{\text{c.m.}}$ can be expressed as

$$\frac{\Delta E_{\text{c.m.}}}{E_{\text{c.m.}}} = \sqrt{\left(\frac{\Delta E_\alpha}{E_\alpha}\right)^2 + 4\left(\frac{\cos(\vartheta_{\text{lab}}) - \cos(\vartheta'_{\text{lab}})}{\cos(\vartheta_{\text{lab}})}\right)^2}, \quad (5)$$

where ΔE_α is the uncertainty in the measured α-particle energy, ϑ_{lab} is the average measured angle, and the uncertainty in the measured angle is $\Delta\vartheta_{\text{lab}} = |\vartheta_{\text{lab}} - \vartheta'_{\text{lab}}|$. In the following illustrative calculations, $E_{\text{c.m.}}$ was varied in 1 MeV increments over the range of 2–6 MeV.

Under the experimental conditions, the energy resolution of the SSD for 4.78-, 5.48-, and 5.795-MeV α particles from a standard source was 103, 98, and 87 keV, respectively. For higher energy α particles, we assumed the resolution of 1.5% as measured for the 5.795-MeV α particles, which should be an overestimate. In an offline test, the SSD resolution for the 5.48-MeV line was as good as 29 keV under vacuum which broadened to 70 keV when the chamber was filled with He + CO$_2$ gas; by folding an assumed 64 keV of broadening from energy straggling with the intrinsic SSD resolution, we were able to reproduce the measured width. Considering the
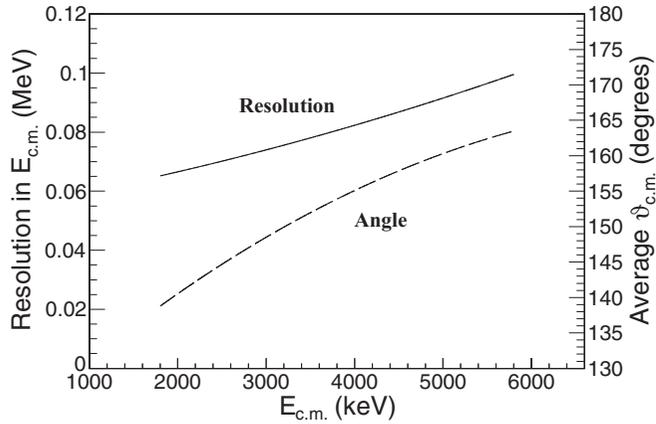
FIG. 8. Uncertainty in determination of the center-of-mass energy $E_{\text{c.m.}}$ in MeV (solid line) and average scattering angle $\vartheta_{\text{c.m.}}$ in degrees (dashed line) as functions of the center-of-mass energy in keV. The range of angles measured in the laboratory frame is roughly $10° \leqslant \vartheta_{\text{lab}} \leqslant 20°$ as $2\vartheta_{\text{lab}} + \vartheta_{\text{c.m.}} = 180°$.

position of the α source was nearly 40 cm from the SSD in offline tests and α particles scattered at an initial laboratory energy of 5.5 MeV would be nearly twice as close to the SSD, 64 keV can be considered the maximum uncertainty for straggling, with higher energy α particles straggling much less as well as originating much closer to the detectors. We finally adopted values for ΔE_α by adding the above SSD resolution and the assumed straggling in quadrature, except for the highest energy α particles where we simply adopted an uncertainty of 1.5% since summing the overestimated uncertainties from both resolution and straggling effects is unreasonable.

In order to estimate the uncertainty in ϑ_{lab} arising from the experimental determination of the scattering position, we need to first estimate the average ϑ_{lab} as a function of $E_{\text{c.m.}}$. We plotted both the laboratory scattering angle ϑ_{lab} and the center-of-mass angle $\vartheta_{\text{c.m.}}$ event by event in order to determine their average values as functions of the center-of-mass energy; the average $\vartheta_{\text{c.m.}}$ is shown in Fig. 8. While the precision of each PPAC to determine a beam particle's position is 0.9 mm in both X and Y, the position resolution becomes 4 mm in both dimensions when extrapolated to a typical scattering depth. The resolution achieved for the α particle's position with the backgammon pads was 3 mm in X and 0.5 mm in Y. All these uncertainties were added together in quadrature to yield a final uncertainty of 6.4 mm in the determination of ϑ_{lab}. A new angle ϑ'_{lab} was calculated by shifting the position of the α particle by the above 6.4 mm, assuming a standard scattering depth Z representative of each of the five center-of-mass energies. The resulting range of $\Delta\vartheta_{\text{lab}}$ was found to be $1.3-2.1°$, increasing with decreasing $E_{\text{c.m.}}$.

Finally, we obtained an estimate for the uncertainty of the center-of-mass energy of about 60–100 keV as shown in Fig. 8; the intrinsic resolution of the SSD had the predominant effect, which was more pronounced at the higher energies. Thus, it can be seen that the energy binning choice of 100 keV is consistent with our achieved resolution.

We confirmed with a simple calculation that the above geometric uncertainties dominate over the uncertainty in the beam energy. Suppose we have two identical measurements, but we know that the incident energy differs between the two beam ions. The result of the kinematic solution is that the optimized scattering depth will be larger for the higher energy beam ion and vice versa for the low energy beam ion, because it is the scattering depth combined with the incident beam energy together that finally determines $E_{\text{c.m.}}$. Assuming a nominal scattering energy of $E_{\text{c.m.}} = 4.0$ MeV, changing the transverse scattering position by the 6.4 mm uncertainty mentioned above is equivalent to $\Delta\vartheta_{\text{lab}} = 1.7°$, changing the scattering depth ΔZ by 27 mm, or changing the beam energy by 5.6 MeV. Thus, the uncertainties of these measurements dominate over the intrinsic spread in the beam energy of 2.0 MeV.

D. *R*-matrix analysis

To extract the resonance parameters of interest, we performed a multilevel, multichannel *R*-matrix calculation [55] with the SAMMY8 code [56]. Succinctly, the *R*-matrix method calculates the interference between the regular and irregular Coulomb functions with physical resonances. The resonances are parameterized by their energy E_r (the same as $E_{\text{c.m.}}$ from elastic scattering as $Q = 0$), channel i partial widths Γ_i, and the angular momenta transfer ℓ_i. The resonance shape is determined by the entrance channel ℓ_α, the resonance height from the entrance channel Γ_α, and the resonance width depends on total width Γ. The total width is a sum of the proton and α partial widths, as both channels are open; the gamma partial widths Γ_γ are negligibly small for these highly excited, particle-unbound states. For the case of $^{30}\text{S} + \alpha$ elastic scattering, the situation is simplified for the entrance channel, as both the nuclei have a ground-state spin parity $J^\pi = 0^+$, and so the quantum selection rules dictate a unique resonance J^π for each ℓ_α value—namely that $J = \ell_\alpha$ and the parity is always natural for populated states in ^{34}Ar.

The calculated excitation function was broadened based on the experimental energy resolution and performed at an average angle of $\vartheta_{\text{c.m.}} = 150°$ as evaluated above in Sec. III C. We quantified the quality of a fit by the reduced chi square χ_ν^2, which is the chi square χ^2 divided by the number of degrees of freedom ν. Fitting the data with pure Coulomb scattering resulted in $\chi_\nu^2 = 4.17$ with 35 degrees of freedom, indicating the possibility for significant improvement could be expected by including the interference effect of resonances in an *R*-matrix fit. As there are no known levels in ^{34}Ar with $E_{\text{ex}} > 11$ MeV, we had to carefully introduce new resonances until the experimental data were reasonably reproduced. The maximum width of a resonance can be estimated with the Wigner limit [57] as

$$W_{\Gamma_i} = \frac{2\hbar^2}{\mu_i R_i^2} P_{\ell_i},\tag{6}$$

where μ is the channel reduced mass, R is the channel radius, and P_ℓ is the channel penetrability, respectively, for channel i. We calculate the penetrability as $P_\ell = \frac{\rho}{F_\ell^2 + G_\ell^2}$, where $\rho = \frac{kR}{\hbar}$ includes the phase space factor k, and F_ℓ and G_ℓ are the

TABLE I. Coupling schemes for states in ^{34}Ar for $J^\pi \leqslant 4^+$ for the ^{33}Cl + p channel. The lowest ℓ_p is assumed, and not all possible linear combinations are denoted. See the text.

J^π	ℓ_p	s	$s_1 \oplus s_2$	$s \oplus \ell$
0^+	2	2	$\uparrow\uparrow$	$\uparrow\downarrow$
1^-	1	2	$\uparrow\uparrow$	$\uparrow\downarrow$
2^+	0	2	$\uparrow\uparrow$	
3^-	1	2	$\uparrow\uparrow$	$\uparrow\uparrow$
4^+	2	2	$\uparrow\uparrow$	$\uparrow\uparrow$

regular and irregular Coulomb functions, respectively. Such a physical constraint is particularly relevant when introducing new resonances to help limit the parameter space. We adopted the channel radius given by $R_i = 1.45(A_1^{1/3} + A_2^{1/3})$ fm, where A_1 and A_2 are the mass numbers of the two species in channel i; an identical parametrization was used in the studies of ^{21}Na + α [58] and ^{26}Si + p [44], which are two of the most similar experiments to the present work. For consistency, the same α-channel radius was also used in the R-matrix calculation.

At the outset, we began with a single channel ($\Gamma = \Gamma_\alpha$), single level manual analysis starting with the lowest-energy features and slowly moving to higher excitation energies in discrete steps of 100 keV. The width was set to the Wigner limit ($\Gamma_\alpha = W_{\Gamma_\alpha}$) to determine which features could be resolved by assuming the existence of a physical resonance. At this time we also checked possible values of the angular momentum transfer ℓ_α; although the experimental setup allowed for values of up to $\ell_\alpha = 6$, $\ell_\alpha \geqslant 5$ never gave good fits, since resonances with these higher transfers are essentially not visible within the present resolution. Only under this condition where $\Gamma_p = 0$ and Γ_α was at the Wigner limit was it possible to observe a change of any kind in the calculation for $E_{c.m.} \leqslant 3.8$ MeV, and even so the calculated deviation from pure Coulomb scattering was of a smaller magnitude than the experimental uncertainty, particularly near 3.5 MeV. The calculations were consistent with our interpretation that the fluctuations below 3.8 MeV are statistical or background induced. The subsequent multilevel, multichannel analysis thus focuses on the region of 3.9–5.6 MeV and assumes $\ell_\alpha \leqslant 4$; three resonancelike structures could be resolved near $E_{c.m.} \approx 4.35$, 4.78, and 5.34 MeV. Although resonances observed by transfer reactions always appear as peaks in the differential cross section, in the case of elastic scattering the interference pattern caused by a resonance can be observed as a diplike structure rather than as a peak, particularly below the Coulomb barrier.

For the proton channel, we assumed the lowest ℓ_p allowed would have the predominant contribution. The spin of the proton $s_1 = \frac{1}{2}$ and the spin of the ^{33}Cl ground state $s_2 = \frac{3}{2}$, which can align ($\uparrow\uparrow$) or antialign ($\uparrow\downarrow$) to give the total spin $s = s_1 \oplus s_2$, and the same is true for the resulting spin s coupling with ℓ_p to sum $J = \ell_p \oplus s$. An example of the lowest-ℓ_p coupling schemes are shown in Table I for up to 4^+ natural-parity states in ^{34}Ar.

For convenience, we introduced the dimensionless reduced partial width $\theta_i^2 = \Gamma_i / W_{\Gamma_i}$, in order to easily ensure that,

regardless of ℓ, $\theta_i^2 \leqslant 1$. Resonant elastic scattering is often analyzed by a single-channel formalism because the resonance shape and height are not affected by the other channels; thus at the outset we simplified our model by controlling the proton width via a universal ratio of the dimensionless reduced partial widths $\xi \equiv \theta_p^2 / \theta_\alpha^2$, which was found to be 3% in a similar work [58]. Although the value of Γ_p derived this way may have a large uncertainty as well as model dependence, it is physically unrealistic to perform a single-channel analysis so far above the proton threshold.

Starting with the first resonance near 4.35 MeV and truncating the excitation function towards higher energies, a computer code optimized E_r, ℓ, θ_α^2, and ξ, until all three resonances were introduced and the fit took into account the entire energy range of the experimental excitation function. Once we had such a reasonable fit ($\xi \approx 4\%$), we then allowed θ_p^2 to vary individually for each resonance and again covaried sets of resonance parameters to search for the best fit for the entire spectrum. In summary, E_r was covaried over 200 keV in 1-keV steps, ℓ was covaried for values over the range of 0–4, θ_α^2 was covaried in 1% steps up to >99%, and θ_p^2 was varied in small increments up to 10% (past where ξ showed poor behavior) in our search for the best fit, shown in Fig. 9(a), where the horizontal errors are from the 100-keV binning and the vertical errors are purely statistical; the absolute magnitude of the statistical error was scaled by the same factor of 2.0 as the data. All possible ℓ values for the 4.78-MeV state are shown in Fig. 9(b) for illustrative purposes.

A number of systematic uncertainties that might affect the differential cross section were carefully considered. These include contributions to each of the parameters in Eq. (4), namely the number density of helium atoms n, the stopping power of the beam $S(E_b)$, the number of injected beam ions I_b, and the changing solid angle $\Delta\Omega$. The number density of ^{4}He atoms in the target employed cannot be changed by any physical argument, since the pressure gauge in the gas flow controller described in Sec. II was consistent with two other pressure gauges. The gas density calculated from the nominal laboratory conditions with the ideal gas law is consistent with the density utilized in all energy loss calculations. Any error in the density of helium would apply equally to CO_2 which induced significant energy loss for the heavy ions. Such energy loss calculations are generally known to be accurate to the order of 10% or better, and moreover we experimentally verified the stopping position and Bragg curve of ^{30}S in the target gas. Although we initially assumed the energy distribution of the ^{30}S ions should be gaussian, we found the centroid was skewed to the low energy side by 1%; calculating the ^{30}S ion incident energy event-by-event based on the rf data rather than assuming a gaussian distribution did not result in any noticeable difference in the elastic scattering excitation function. The number of incident ^{30}S ions is determined in part by the PPAC scalers, the magnitude of which can be confirmed as we recorded a downscaled spectrum of the cocktail beam; although the latter is less accurate, the two methods agreed within 6%. We checked the method of calculating the solid angle, as well as the absolute efficiency of the silicon detectors, considering the known intensity of the standard α source used in off-line calibration runs; within the errors of these
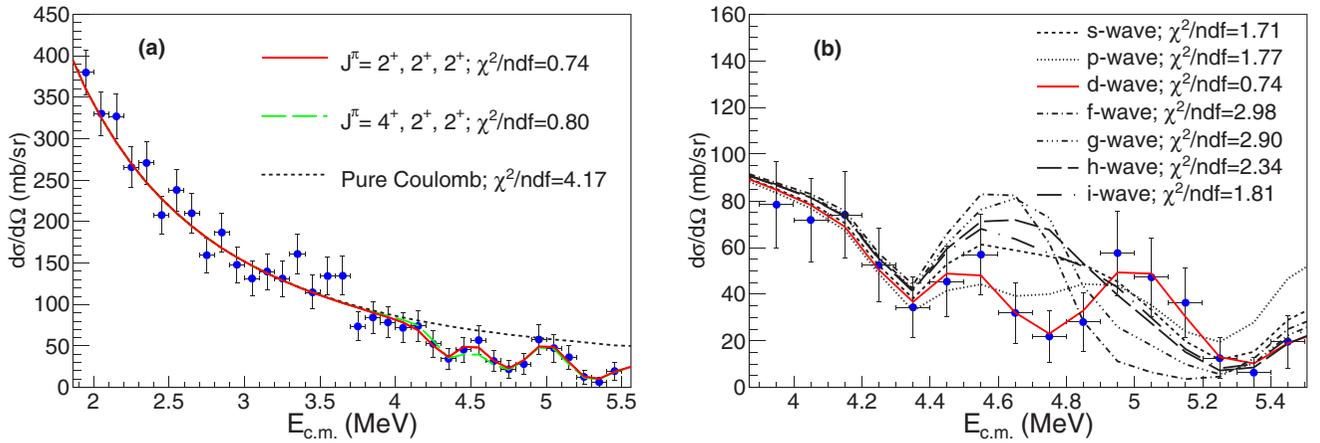
FIG. 9. ^{30}S + α elastic scattering excitation function including fits. (a) The energy range displayed is the entire set of continuous data in the raw excitation function, except at the lower energy side where the plot is terminated at the point where all the α particles can no longer reach the detector from stopping in the fill gas. The bumps observed around 3.5 MeV correspond to a region of large α background, as depicted in Fig. 7. Three resonancelike structures are seen at 4.0 MeV $< E_{\mathrm{c.m.}} <$ 5.5 MeV. The data are fit with a multichannel (α and p), multilevel R-matrix formalism, and the results for a selected combination of ℓ_α transfers are shown (though all combinations up to $\ell_\alpha \leqslant 4$ were tested, and $\ell_\alpha = 5,6$ never gave good fits). The adopted parameters of these three newly discovered resonances are shown in Table II. (b) All physically allowed ℓ_α values for the $E_r = 4.78$ MeV resonance, showing the unambiguous assignment of $\ell = 2$. See the text.

calculations, we found the efficiency $\eta > 99\%$ for the relevant silicon detectors before and after the experimental run, indicating the detectors were not damaged during the experiment. As the scaling factor of 2.0 ± 0.1 is the main source of systematic error, we take its associated uncertainty of 5% as the systematic uncertainty in the present work. Because the statistical error is $\geqslant 25\%$ over the resonant-dominated region, the systematic error makes a negligible contribution to the final error evaluation.

The resonance parameters deduced from the R-matrix analysis are shown in Table II. The uncertainties in the adopted level parameters were calculated in the following ways. For the excitation energy E_{ex}, we used the experimental energy resolution as discussed in Sec. III C and shown in Fig. 8. The error of the remaining level parameters was evaluated considering the range where an individual parameter is allowed to vary within one standard deviation of the best fit χ_ν^2; the same method was used over the range of $E_{\mathrm{c.m.}}$ 1.9–4.1 MeV with pure Rutherford scattering to determine the scaling factor and its error of 2.0 ± 0.1. The recommended spin parity J^π is given, and any other spin parity which is possible is listed, as are the associated widths in their respective columns separated by commas. The error in Γ_p is seen to be generally larger than in Γ_α, because the α elastic scattering resonant structure is

much less sensitive to the proton channel compared to the α channel.

The resonance parameters obtained in the present study appear to be reasonable except for the widths for the 12.08-MeV state. In particular, the 12.08-MeV state's structure cannot be a pure α cluster which also has a non-negligible proton decay branch. Our favored interpretation is that there are one or more unresolved resonances with substantial α-cluster configuration in this region. Moreover, the behavior of the resonance tail is unconstrained by the data, and any interference effects from unknown physical resonances outside the energy range cannot be accounted for. Thus, there are large systematic uncertainties associated with the resonance parameters extracted from an R-matrix fit for states near the boundary of the experimental energy range. However, it cannot be doubted that the data indicate one or more very strong α-cluster resonance(s) in this region of excitation energy, which is a point we emphasize in our discussion of these results below.

IV. DISCUSSION

We observed the signature interference patterns of several resonances in ^{34}Ar with large α partial widths Γ_α via α elastic scattering on ^{30}S. The cluster threshold rule predicts

TABLE II. Best fit level parameters of ^{34}Ar determined by the present work. All levels are newly proposed. The table is arranged such that the corresponding physical property of each state in ^{34}Ar precedes the corresponding R-matrix fit parameter. As we could not uniquely constrain the spin parity of the 11.09-MeV level, two possible assignments are given, as well as the corresponding widths. The 12.08-MeV level is shown in italic letters as there is a large systematic uncertainty associated with it. See the text.

E_{ex} (MeV)	E_r (MeV)	J^π	ℓ_α	Γ_α (keV)	θ_α^2 (%)	Γ_p (keV)	ξ (%)
11.092(85)	4.353(85)	$(2^+,4^+)$	2, 4	$20^{+80}_{-17}, 0.5^{+1.4}_{-0.4}$	$40^{+180}_{-33}, 8^{+10}_{-6}$	$25^{+500}_{-20}, 0.3^{+3.5}_{-0.3}$	1, 0.1
11.518(89)	4.779(89)	2^+	2	100^{+120}_{-60}	90^{+110}_{-55}	210^{+600}_{-170}	4
12.079(95)	*5.340(95)*	*(2^+)*	*2*	*260^{+400}_{-120}*	*100^{+150}_{-45}*	*340^{+550}_{-200}*	*6*

the existence of these states, which have a large overlap of the cluster configuration to the nuclear wave function nearby the respective cluster's separation energy [59,60]. Such α-cluster resonances have typically dominated the stellar rate of exothermic $(α,n)$ and $(α,p)$ reactions on $T_z = ±1$ nuclei, respectively, when they fall within the astrophysical Gamow burning window [61]. α resonant elastic scattering has long been known as a powerful tool to selectively observe states with large $Γ_α$. The effect is especially pronounced in inverse kinematics, where measurements at large backward angles are possible and the nonresonant cross sections are minimized; under these conditions, one expects to observe states with $Γ_α$ comparable to the experimental energy resolution [33]. According to calculations of the Wigner limit [see Eq. (6)], the maximum theoretical width shrinks rapidly as the energy is reduced towards the threshold.

Our observation that all three resonances are consistent with a 2^+ assignment may make one wonder if there is a reason for such behavior. These may be regarded as a triplet if the tentative assignments of 2^+ are correct for both the 11.09- and 12.08-MeV states. Alternatively, our 11.51-MeV state could be regarded as a 2^+ doublet paired with either these other two states. We note that all three are observed as diplike structures, so it may not be surprising that features in the differential cross section with similar interference patterns can result from physical resonances with the same $J^π$. A system of α-cluster doublets was observed in the $T_z = +1$ nucleus ^{22}Ne [62,63] with $J^π$ correlated with increasing energy, albeit for states of negative rather than positive parity. Unfortunately, comparison with model predictions is still a challenge for the ^{30}S mass region.

A. Reaction rate

The peak temperature of x-ray bursts is expected to be in the range of 1.3–2 GK corresponding to the Gamow burning windows of $1.7 \lesssim E_{c.m.} \lesssim 3.8$ MeV. To make a meaningful evaluation of the stellar reaction rate in XRBs, we therefore need to consider not only the resonances discovered in the present work, but also ^{34}Ar states at lower E_{ex}. In fact, before the present work there has never been an evaluation of the ^{30}S$(α,p)$ cross section based on experimental level structure of ^{34}Ar owing to the paucity of such data and the experimental challenges of studies in this region of the periodic table.

The ^{36}Ar$(p,t)^{34}$Ar measurement performed at the Research Center for Nuclear Physics (RCNP), Osaka University, observed resonances above the α threshold at a relatively smooth interval—about four resonances per MeV—over four MeV in excitation energy [31]. Considering the significant difference in energy resolution, our observation of three (or four, depending on the interpretation of our 12.08-MeV state) resonances per MeV over the range of our experimental energy and as the resolution allows, there is a basic consistency between the two studies, which both only populate natural-parity states.[2]

However, the results from the RCNP spectroscopic study only provides us with preliminary resonance energies, and some assumptions are required before we may apply them. First, we naïvely assumed that each state has $J^π = 0^+$. As for the partial widths, based on the present results and the similar level density between the two studies, we set $Γ_α = \frac{1}{2}W_{Γ_α}$. Although our $θ_α^2$ are generally larger than 0.5 according to Table II, setting $θ_α^2 ≈ 1$ for such a large series of resonances would be unusual considering $Γ_p ≠ 0$ and thus $Γ > Γ_α$ and hence $θ_α^2 < 1$. We believe a factor of 0.5 is still rather extreme but more reasonable.

It should be noted a thorough analysis of the RCNP experimental data would only improve the situation with regard to the precision of the excitation energies (or the removal of any states which are background induced) and not the spin parities nor the partial widths. The limited angular distribution available from their spectrometer does not cover a full phase for reliable comparison with a DWBA calculation [65,66].

We calculated the resonant reaction rate per particle pair $⟨σv⟩$ using the standard formulation [57] which depends only on the resonance energies E_r, spins J, and the channel partial widths $Γ_i$. The spin comes into play in the spin statistical factor $ω$ as

$$ω ≡ \frac{2J_r + 1}{(2J_A + 1)(2J_a + 1)}, \qquad (7)$$

where $J_{A,a}$, the spins of the two nuclei in the entrance channel, are both zero in the case of ^{30}S + α. The reduced width $γ$ is defined as

$$γ ≡ \frac{Γ_a Γ_b}{Γ_{tot}}, \qquad (8)$$

for the entrance and exit channel partial widths $Γ_{a,b}$, respectively. Their product $ωγ$ is called the resonance strength as it is proportional to the integral of the resonance cross section. We also use the standard simplification that $γ = (Γ_α Γ_p)/(Γ_α + Γ_p) ≈ Γ_α$ when $Γ_α \ll Γ_p$, which is a realistic assumption considering the vastly different Wigner limits of the two channels.[3] The resulting $ωγ$ for each resonance in the ^{36}Ar(p,t) study based on our assumptions that $J = 0$ and $γ = Γ_α = \frac{1}{2}W_{Γ_α}$ varies by only a factor of around 2 for $J \leqslant 3$ (although it quickly drops off for $J \geqslant 5$) as shown in Fig. 10, vindicating our arbitrary treatment of the spin in our framework; $ωγ$ is independent of low J to first order because we parametrize the width based on the Wigner limit, which decreases with increasing J, whereas for the ^{30}S + α entrance channel $ω = 2J_r + 1$. While the properties of an individual resonance calculated in this manner will be unreliable, the sum of these contributions can be considered an upper limit under extreme assumptions on the nuclear structure of ^{34}Ar.

---

[2]While a single step (p,t) transfer reaction can only populate natural-parity states, a multistep process allows for the population of unnatural-parity states (see, e.g., Ref. [64]). However, the cross section to populate unnatural-parity states by a multistep process is

significantly smaller than the cross section for a single step process as a general rule.

[3]According to our data from Table II, the best fit $Γ_p$ and $Γ_α$ are of comparable size. However, we note that the upper-limit errors for $Γ_p$ are extremely large, which is not inconsistent with the assumption that $γ ≈ Γ_α$. Even in the case that $Γ_α = Γ_p$, $γ = \frac{1}{2}Γ_α$, giving a similar factor of 2 error to $ωγ$ as the assumption of $J = 0$ as shown presently.
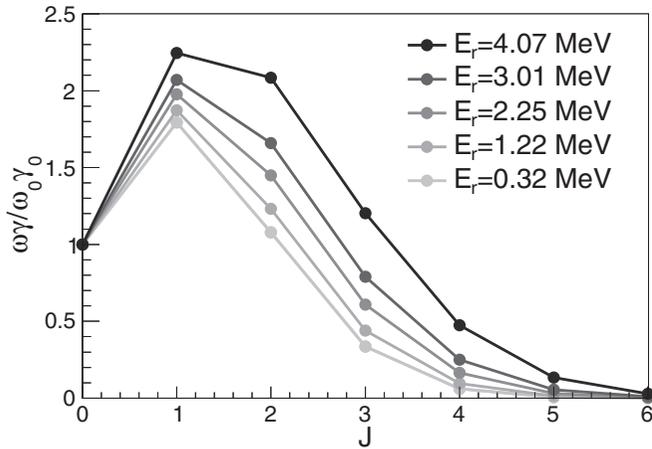
FIG. 10. Relative dependence of the resonance strength $\omega\gamma$ from individual states based on their spin J under the assumption that $\gamma \approx \Gamma_\alpha \propto W_{\Gamma_\alpha}$. The resonance strengths are normalized to the case of $J = 0$, denoted as $\omega_0\gamma_0$. The $E_r = 2.25$-MeV state is the closest to the center of the 1.3-GK Gamow window.

Our goal here is to provide an evaluation of the ^{30}S(α, p) reaction rate in x-ray bursts by assuming broad widths for all the known states in ^{34}Ar near the astrophysically interesting region. According to Fig. 10, the choice of $J^\pi = 0^+$ yields a median value of the resonance strength for low J in our model and thus represents the physically realistic case where there are a multitude of different spins among the levels in ^{34}Ar over the α threshold. It can be seen in the case of $J = 3$ or higher that the reaction rate could be half or less than our suggested

upper limit. To demonstrate, we considered the case when $\gamma = \Gamma_\alpha = 2W_{\Gamma_\alpha}$ and $J^\pi = 4^+$; between $T = 1$ and 3 GK the reaction rate is a factor of 2 *lower* than our evaluation in spite of the fact that the reduced width was twice rather than half the Wigner limit. This feature of the Wigner limit is satisfyingly consistent with the fact that resonant thermonuclear reaction rates tend to be dominated by lower partial wave contributions because the angular momentum barrier is smaller. Importantly, the rate only exceeds our evaluation by 0.2% at $T = 1.5$ GK if we allow the maximum Γ_α from our experimental uncertainties in Table II, which we consider to be a trivial difference.

The ^{34}Ar resonance parameters adopted for our ^{30}S(α, p) stellar reaction rate calculation are listed in Table III along with calculations of the proton and α Wigner limits. We used the graph digitizing system GSYS from the Hokkaido University Nuclear Reaction Data Centre, which was developed specifically for extracting numerical nuclear data from published spectra, to obtain the resonance energies from the ^{36}Ar(p,t) study [31]. For the known resonances, we found deviations from the compiled level scheme [68] of at most around 30 keV, which is the same as the experimental error quoted by O'Brien *et al.* The resulting stellar reaction rate is shown in Fig. 11 in comparison to a statistical model (SM) rate [67]. As this is the first ^{30}S(α, p) reaction rate based on the experimental level structure of ^{34}Ar, there are not many other studies to compare ours against. The two most relevant studies are the ^{33}Cl(p, α) measurement [32] and a recent survey of α-induced cross sections for masses $A \approx 20-50$ [69].

In order to compare the present results with the time-reversal study by Deibel *et al.* [32], one should keep in mind that the ^{30}S(α, p) Q value is 2.080 MeV, and thus their energy range

TABLE III. Resonance parameters of ^{34}Ar adopted in the calculation of the ^{30}S(α, p) stellar reaction rate calculation. Resonances with $E_r < 0.7$ MeV are not tabulated as they fall below the x-ray burst Gamow window and the Wigner limit for the α channel rapidly vanishes. Parameters shown in boldface are based on experimental data. Level energies below $E_{ex} < 11$ MeV are taken from Ref. [31], where we assumed $J^\pi = 0^+$ and $\Gamma_\alpha = \frac{1}{2}W_{\Gamma_\alpha} = \gamma$; the relative dependence of J and γ for small J in our framework is exemplified in Fig. 10. The higher energy resonances are from the present work and are separated from the others by a horizontal rule. We stress that the tabulated properties which are not taken from experimental data may not be correct for individual resonances, but rather that the sum of these contributions to the stellar reaction rate can be considered an upper limit under an extreme assumption, which is interesting to investigate. See the text.

E_{ex} (MeV)	E_r (MeV)	J^π	ω	Γ_α (keV)	W_{Γ_α} (keV)	W_{Γ_p} (MeV)	$\omega\gamma$ (keV)
7.47	**0.73**	(0$^+$)	1	2×10^{-15}	4×10^{-15}	2×10^{-1}	2×10^{-15}
7.88	**1.14**	(0$^+$)	1	2×10^{-9}	3×10^{-9}	4×10^{-1}	2×10^{-9}
7.96	**1.22**	(0$^+$)	1	1×10^{-8}	2×10^{-8}	4×10^{-1}	1×10^{-8}
8.15	**1.41**	(0$^+$)	1	4×10^{-7}	8×10^{-7}	6×10^{-1}	4×10^{-7}
8.30	**1.56**	(0$^+$)	1	4×10^{-6}	8×10^{-6}	6×10^{-1}	4×10^{-6}
8.55	**1.81**	(0$^+$)	1	1×10^{-4}	2×10^{-4}	8×10^{-1}	1×10^{-4}
8.74	**2.0**	(0$^+$)	1	7×10^{-4}	1×10^{-3}	9×10^{-1}	7×10^{-4}
8.89	**2.15**	(0$^+$)	1	3×10^{-3}	5×10^{-3}	1	3×10^{-3}
8.99	**2.25**	(0$^+$)	1	7×10^{-3}	0.01	1	7×10^{-3}
9.42	**2.68**	(0$^+$)	1	0.1	2	1	0.1
9.75	**3.01**	(0$^+$)	1	0.7	1	2	0.7
10.32	**3.58**	(0$^+$)	1	7	10	2	7
10.81	**4.07**	(0$^+$)	1	30	50	3	30
11.09	**4.35**	**2$^+$**	5	**20**	50	5	100
11.52	**4.78**	**2$^+$**	5	**100**	110	5	500
12.08	**5.34**	**2$^+$**	5	**260**	260	6	1300
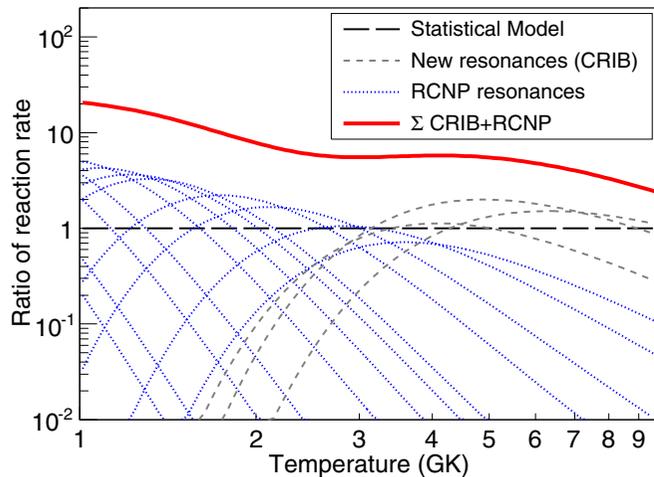
FIG. 11. Calculations of the ^{30}S(α,p) stellar reaction rate from 1–10 GK. The statistical model (SM) rate from NON-SMOKER [67] is shown as the long-dashed black line, to which all the rates are normalized. The dashed grey lines represent our new higher-energy resonances observed at CRIB with our best fit quantum properties. The dotted (blue) lines represent the 13 resonances from the ^{36}Ar(p,t) RCNP experiment [31], where we made a couple of assumptions about their quantum properties. The sum of these individual resonant contributions is shown as the thick solid (red) line. The adopted individual resonance properties are listed in Table III.

in ^{30}S + α is $4.09 \leqslant E_{\text{c.m.}} \leqslant 5.35$ MeV (as shown in their Table I), quite similar to the range of resonances observed in the present work. The previous study includes only the (α, p_0) ground-state component, whereas the present Γ_p does not exclude the summed contribution from all states where the assumption $\Gamma_\alpha \ll \Gamma_{p_i}$ remains valid for at least one p_i; the SM rate implicitly includes transitions to allowed states. The present work shows an enhancement of around a factor of 5 over the SM rate as an upper limit, and the work of Deibel *et al.* shows a ^{30}S(α_0, p_0) cross section which is more comparable to the SM rate and is considered as a lower limit to the total (α, p) cross section. Even if one only includes the resonances we observed at CRIB, it can be seen that near 3 GK our three resonances alone are quite similar to the SM rate.

The reduction scheme presented by Mohr generally shows a global behavior of the cross sections for (α, p) and (α, n) reactions over a large energy range for medium mass nuclei [69]. Specifically, most of the experimental data can be reproduced by a SM calculation. However, deviations higher than the expected cross sections were found in some of the measurements with ^{23}Na and ^{33}S, whereas the species ^{36}Ar and ^{40}Ar were seen to be much lower (at least for the available data). For the case of ^{23}Na, the work of Mohr motivated the community to reinvestigate the ^{23}Na(α, p) cross section, which was finally found to be consistent with the SM calculation within the experimental uncertainties [70–73]. In the outstanding cases, these discrepancies certainly warrant further investigation to determine if they are real or artificial (see also the discussion in the recent work by Anderson *et al.* [74]). If the effects are real, ^{30}S is seen to fall within the mass
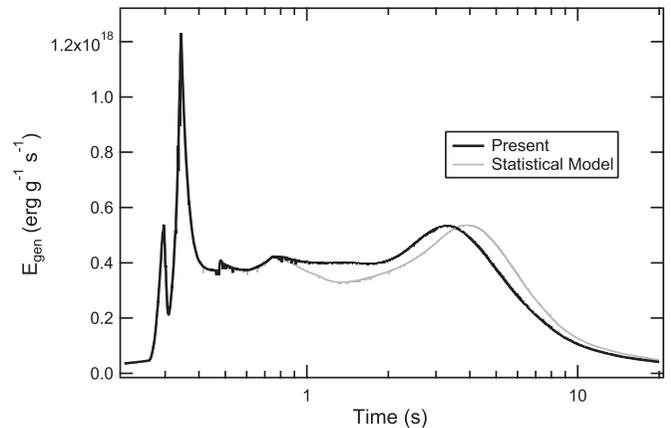
FIG. 12. Nuclear energy generation rates during one-zone XRB calculations using the K04 thermodynamic history [13]. Results using the present rate (black line) and a statistical model rate [67] (grey line) are indicated.

range where there is a cross section enhancement over the SM, which supports the findings of the present study.

B. Astrophysical implications

The impact of our new upper limit for the ^{30}S$(\alpha,p)^{33}$Cl rate was examined within the framework of one-zone XRB postprocessing calculations using the K04 ($T_{\text{peak}} = 1.4$ GK) model [13]. As shown in Fig. 12, striking differences in the profiles of nuclear energy generation rates between approximately 1 and 10 s are seen when comparing XRB calculations using the present upper limit and a statistical model rate calculation [67] (see Fig. 11). Indeed, E_{gen} differs by as much as 25% between calculations using these two rates. Nucleosynthesis predictions are also affected by the particular ^{30}S(α,p) rate adopted in the calculations. Comparing results using the present upper limit and the statistical model rate, abundance differences of up to 30% are observed for species with mass fractions $> 10^{-6}$ (summed over mass number) for A over the rather broad range of approximately $20-80$. Further tests using full hydrodynamic XRB models are needed to explore in detail the possible dramatic impact of the ^{30}S$(\alpha,p)^{33}$Cl rate on predictions of XRB observables.

V. SUMMARY

We observed several resonances with large α widths in the energy range $E_{\text{ex}} = 11.1 - 12.1$ MeV for the first time in ^{34}Ar via the α resonant elastic scattering of ^{30}S and determined their properties of spin, parity, and widths. Using our new data, we were able to make the first-ever calculation of the astrophysical ^{30}S(α,p) cross section based on the experimental level structure of ^{34}Ar. Although these resonances do not seem to have a large effect for the astrophysically interesting energies important for XRBs, we could set a reasonable upper limit on the stellar reaction rate of about one order of magnitude greater than the Hauser-Feshbach statistical model. The resonances we observed correspond very well to the energy range covered in the time-reversal study. These two studies complement each other nicely, as our work provides an upper limit to the

cross section, which we determined to be somewhat above the existing ^{33}Cl(p_0, α_0) lower limit to the total ^{30}S(α, p) cross section. Although the present knowledge of the level structure of ^{34}Ar, as well as the ^{30}S(α, p) cross section, at the most astrophysically interesting temperatures remains elusive, our new upper limit can, for the first time, conclusively rule out the artificial cross section enhancement of a factor of a hundred over the SM used in one XRB model [16]. This can, in turn, rule out the influence of the ^{30}S(α, p) reaction in explaining such double-peaked burst morphology, consistent with the theoretical findings of a recent study [17].

From a technical perspective, we developed the highest quality ^{30}S radioactive ion beam for astrophysical studies yet in the world. Our analysis also showed that active target systems must be designed with extremely high precision capabilities and that reports of α scattering with such systems must be viewed with scrutiny. However, the active target system enabled us to understand the energy loss properties of the beam very clearly, which is often a challenge for experiments performed using a thick target in inverse kinematics.

Further work is required to elucidate the behavior of the ^{30}S(α, p) stellar reaction rate over the energy ranges applicable to XRBs so that its predicted influence on the energy generation, compositional inertia, and burst light curve can be reliably extracted from theoretical models. Of course, a direct measurement of the ^{30}S(α, p) reaction at the relevant energies would be the ideal approach, but it is unclear when a sufficiently intense, low energy ^{30}S RIB will become available. An intensity like 10^4 pps is insufficient, and it took us four years to develop such an RIB for the present study. Instead, the community should continue to exploit indirect methods as in the present study in the near future. In particular, it is critical to obtain more experimental knowledge of the quantum properties, particularly Γ_α, of states in ^{34}Ar over E_{ex} from 8.0 to 11.5 MeV.

[1] D. K. Galloway, M. P. Muno, J. M. Hartman, D. Psaltis, and D. Chakrabarty, Astrophys. J. Suppl. **179**, 360 (2008).

[2] W. H. G. Lewin, Mon. Not. R. Astron. Soc. **179**, 43 (1977).

[3] S. Ayasli and P. C. Joss, Astrophys. J. **256**, 637 (1982).

[4] H. Schatz, A. Aprahamian, V. Barnard, L. Bildsten, A. Cumming, M. Ouellette, T. Rauscher, F.-K. Thielemann, and M. Wiescher, Phys. Rev. Lett. **86**, 3471 (2001).

[5] S. E. Woosley, A. Heger, A. Cumming, R. D. Hoffman, J. Pruet, T. Rauscher, J. L. Fisker, H. Schatz, B. A. Brown, and M. Wiescher, Astrophys. J. Suppl. **151**, 75 (2004).

[6] H. Schatz and K. E. Rehm, Nucl. Phys. A **777**, 601 (2006).

[7] J. L. Fisker, H. Schatz, and F.-K. Thielemann, Astrophys. J. Suppl. **174**, 261 (2008).

[8] A. Parikh, J. José, G. Sala, and C. Iliadis, Prog. Part. Nucl. Phys. **69**, 225 (2013).

[9] A. E. Champagne and M. Wiescher, Annu. Rev. Nucl. Part. Sci. **42**, 39 (1992).

[10] W. H. G. Lewin, J. van Paradijs, and R. E. Taam, Space Sci. Rev. **62**, 223 (1993).

[11] M. Wiescher, J. Görres, and H. Schatz, J. Phys. G: Nucl. Phys. **25**, 133 (1999).

[12] R. K. Wallace and S. E. Woosley, Astrophys. J. Suppl. **45**, 389 (1981).

[13] A. Parikh, J. José, F. Moreno, and C. Iliadis, Astrophys. J. Suppl. **178**, 110 (2008).

[14] R. E. Taam, Astrophys. J. **241**, 358 (1980).

[15] C. Iliadis, P. M. Endt, N. Prantzos, and W. J. Thompson, Astrophys. J. **524**, 434 (1999).

[16] J. L. Fisker, F.-K. Thielemann, and M. Wiescher, Astrophys. J. **608**, L61 (2004).

[17] R. H. Cyburt, A. M. Amthor, A. Heger, E. Johnson, L. Keek, Z. Meisel, H. Schatz, and K. Smith, Astrophys. J. **830**, 55 (2016).

[18] A. Heger, A. Cumming, D. K. Galloway, and S. E. Woosley, Astrophys. J. **671**, L141 (2007).

[19] D. K. Galloway, A. Cumming, E. Kuulkers, L. Bildsten, D. Chakrabarty, and R. E. Rothschild, Astrophys. J. **601**, 466 (2004).

[20] F. Özel, Nature (London) **441**, 1115 (2006).

[21] F. Özel, A. Gould, and T. Güver, Astrophys. J. **748**, 5 (2012).

[22] T. Güver, F. Özel, A. Cabrera-Lavers, and P. Wroblewski, Astrophys. J. **712**, 964 (2010).

[23] M. Zamfir, A. Cumming, and D. K. Galloway, Astrophys. J. **749**, 69 (2012).

[24] M. Notani, S. Kubono, T. Teranishi, Y. Yanagisawa, S. Michimasa, K. Ue, J. J. He, H. Iwasaki, H. Baba, M. Tamaki, T. Minemura, S. Shimoura, N. Hokoiwa, Y. Wakabayashi, T. Sasaki, T. Fukuchi, A. Odahara, Y. Gono, Z. Fülöp, E. K. Lee *et al.*, Nucl. Phys. A **746**, 113 (2004).

[25] C. Fu, V. Z. Goldberg, A. M. Mukhamedzhanov, G. G. Chubarian, G. V. Rogachev, B. Skorodumov, M. McCleskey, Y. Zhai, T. Al-Abdullah, G. Tabacaru, L. Trache, and R. E. Tribble, Phys. Rev. C **76**, 021603 (2007).

[26] A. Kim, N. H. Lee, M. H. Han, J. S. Yoo, K. I. Hahn, H. Yamaguchi, D. N. Binh, T. Hashimoto, S. Hayakawa, D. Kahl, T. Kawabata, Y. Kurihara, Y. Wakabayashi, S. Kubono, S. Choi, Y. K. Kwon, J. Y. Moon, H. S. Jung, C. S. Lee, T. Teranishi *et al.*, Phys. Rev. C **92**, 035801 (2015).

[27] W. Bradfield-Smith, T. Davinson, A. DiPietro, A. M. Laird, A. N. Ostrowski, A. C. Shotter, P. J. Woods, S. Cherubini, W. Galster, J. S. Graulich, P. Leleux, L. Michel, A. Ninane, J. Vervier, J. Görres, M. Wiescher, J. Rahighi, and J. Hinnefeld, Phys. Rev. C **59**, 3402 (1999).

[28] D. Groombridge, A. C. Shotter, W. Bradfield-Smith, S. Cherubini, T. Davinson, A. DiPietro, J. Görres, J. S. Graulich, A. M. Laird, P. Leleux, A. Musumarra, A. Ninane, A. N. Ostrowski, J. Rahighi, H. Schatz, M. Wiescher, and P. J. Woods, Phys. Rev. C **66**, 055802 (2002).

[29] J. Hu, J. J. He, A. Parikh, S. W. Xu, H. Yamaguchi, D. Kahl, P. Ma, J. Su, H. W. Wang, T. Nakao, Y. Wakabayashi, T. Teranishi, K. I. Hahn, J. Y. Moon, H. S. Jung, T. Hashimoto, A. A. Chen, D. Irvine, C. S. Lee, and S. Kubono, Phys. Rev. C **90**, 025803 (2014).

[30] L. Y. Zhang, J. J. He, A. Parikh, S. W. Xu, H. Yamaguchi, D. Kahl, S. Kubono, P. Mohr, J. Hu, P. Ma, S. Z. Chen, Y. Wakabayashi, H. W. Wang, W. D. Tian, R. F. Chen, B. Guo, T. Hashimoto, Y. Togano, S. Hayakawa, T. Teranishi *et al.*, Phys. Rev. C **89**, 015804 (2014).

[31] S. O'Brien, T. Adachi, G. P. A. vandenBerg, M. Couder, M. Dozono, H. Fujita, Y. Fujita, J. Görres, K. Hatanaka, D. Ishikawa, T. Kubo, H. Matsubara, Y. Namiki, Y. Ohkuma, H. Okamura, H. J. Ong, D. Patel, Y. Sakemi, K. Sault, Y. Shimbara *et al.*, in *Capture Gamma-Ray Spectroscopy and Related Topics: Proceedings of the 13th International Symposium on Capture Gamma-Ray Spectroscopy and Related Topics*, edited by J. Jolie, A. Zilges, N. Warr, and A. Blazhev, AIP Conf. Proc. No. 1090 (AIP, Melville, NY, 2009), p. 288.

[32] C. M. Deibel, K. E. Rehm, J. M. Figueira, J. P. Greene, C. L. Jiang, B. P. Kay, H. Y. Lee, J. C. Lighthall, S. T. Marley, R. C. Pardo, N. Patel, M. Paul, C. Ugalde, A. Woodard, A. H. Wuosmaa, and G. Zinkann, Phys. Rev. C **84**, 045802 (2011).

[33] K. P. Artemov, O. P. Belyanin, A. L. Vetoshkin, R. Wolskj, M. S. Golovkov, V. Z. Gol'dberg, M. Madeja, V. V. Pankratov, I. N. Serikov, V. A. Timofeev, V. N. Shadrin, and J. Szmider, Sov. J. Nucl. Phys. **52**, 408 (1990).

[34] S. Kubono, Y. Yanagisawa, T. Teranishi, S. Kato, Y. Kishida, S. Michimasa, Y. Ohshiro, S. Shimoura, K. Ue, S. Watanabe, and N. Yamazaki, Eur. Phys. J. A **13**, 217 (2002).

[35] Y. Yanagisawa, S. Kubono, T. Teranishi, K. Ue, S. Michimasa, M. Notani, J. J. He, Y. Ohshiro, S. Shimoura, S. Watanabe, N. Yamazaki, H. Iwasaki, S. Kato, T. Kishida, T. Morikawa, and Y. Mizoi, Nucl. Instrum. Methods Phys. Res., Sect. A **539**, 74 (2005).

[36] T. Teranishi, S. Kubono, S. Shimoura, M. Notani, Y. Yanagisawa, S. Michimasa, K. Ue, H. Iwasaki, M. Kurokawa, Y. Satou, T. Morikawa, A. Saito, H. Baba, J. H. Lee, C. S. Lee, Z. Fülöp, and S. Kato, Phys. Lett. B **556**, 27 (2003).

[37] T. Teranishi, S. Kubono, H. Yamaguchi, J. J. He, A. Saito, H. Fujikawa, G. Amadio, M. Niikura, S. Shimoura, Y. Wakabayashi, S. Nishimura, M. Nishimura, J. Y. Moon, C. S. Lee, A. Odahara, D. Sohler, L. H. Khiem, Z. H. Li, G. Lian, and W. P. Liu, Phys. Lett. B **650**, 129 (2007).

[38] H. Yamaguchi, Y. Wakabayashi, S. Kubono, G. Amadio, H. Fujikawa, T. Teranishi, A. Saito, J. J. He, S. Nishimura, Y. Togano, Y. K. Kwon, M. Niikura, N. Iwasa, K. Inafuku, and L. H. Khiem, Phys. Lett. B **672**, 230 (2009).

[39] J. J. He, S. Kubono, T. Teranishi, M. Notani, H. Baba, S. Nishimura, J. Y. Moon, M. Nishimura, H. Iwasaki, Y.

Yanagisawa, N. Hokoiwa, M. Kibe, J. H. Lee, S. Kato, Y. Gono, and C. S. Lee, Phys. Rev. C **76**, 055802 (2007).

[40] J. J. He, S. Kubono, T. Teranishi, M. Notani, H. Baba, S. Nishimura, J. Y. Moon, M. Nishimura, S. Michimasa, H. Iwasaki, Y. Yanagisawa, N. Hokoiwa, M. Kibe, J. H. Lee, S. Kato, Y. Gono, and C. S. Lee, Eur. Phys. J. A **36**, 1 (2008).

[41] J. J. He, S. Kubono, T. Teranishi, J. Hu, M. Notani, H. Baba, S. Nishimura, J. Y. Moon, M. Nishimura, H. Iwasaki, Y. Yanagisawa, N. Hokoiwa, M. Kibe, J. H. Lee, S. Kato, Y. Gono, and C. S. Lee, Phys. Rev. C **80**, 015801 (2009).

[42] A. Kim, N. H. Lee, I. S. Hahn, J. S. Yoo, M. H. Han, S. Kubono, H. Yamaguchi, S. Hayakawa, Y. Wakabayashi, D. Binh, H. Hashimoto, T. Kawabata, D. Kahl, Y. Kurihara, Y. K. Kwon, T. Teranishi, S. Kato, T. Komatsubara, B. Guo, G. Bing *et al.*, J. Korean Phys. Soc. **57**, 40 (2010).

[43] H. Yamaguchi, T. Hashimoto, S. Hayakawa, D. N. Binh, D. Kahl, S. Kubono, Y. Wakabayashi, T. Kawabata, and T. Teranishi, Phys. Rev. C **83**, 034306 (2011).

[44] H. S. Jung, C. S. Lee, Y. K. Kwon, J. Y. Moon, J. H. Lee, C. C. Yun, S. Kubono, H. Yamaguchi, T. Hashimoto, D. Kahl, S. Hayakawa, S. Choi, M. J. Kim, Y. H. Kim, Y. K. Kim, J. S. Park, E. J. Kim, C.-B. Moon, T. Teranishi, Y. Wakabayashi *et al.*, Phys. Rev. C **85**, 045802 (2012).

[45] J. Chen, A. A. Chen, G. Amádio, S. Cherubini, H. Fujikawa, S. Hayakawa, J. J. He, N. Iwasa, D. Kahl, L. H. Khiem, S. Kubono, S. Kurihara, Y. K. Kwon, M. La Cognata, J. Y. Moon, M. Niikura, S. Nishimura, J. Pearson, R. G. Pizzone, T. Teranishi *et al.*, Phys. Rev. C **85**, 015805 (2012).

[46] H. Yamaguchi, D. Kahl, Y. Wakabayashi, S. Kubono, T. Hashimoto, S. Hayakawa, T. Kawabata, N. Iwasa, T. Teranishi, Y. K. Kwon, D. N. Binh, L. H. Khiem, and N. N. Duy, Phys. Rev. C **87**, 034303 (2013).

[47] S. J. Jin, Y. B. Wang, J. Su, S. Q. Yan, Y. J. Li, B. Guo, Z. H. Li, S. Zeng, G. Lian, X. X. Bai, W. P. Liu, H. Yamaguchi, S. Kubono, J. Hu, D. Kahl, H. S. Jung, J. Y. Moon, C. S. Lee, T. Teranishi, H. W. Wang *et al.*, Phys. Rev. C **88**, 035801 (2013).

[48] J. J. He, L. Y. Zhang, A. Parikh, S. W. Xu, H. Yamaguchi, D. Kahl, S. Kubono, J. Hu, P. Ma, S. Z. Chen, Y. Wakabayashi, B. H. Sun, H. W. Wang, W. D. Tian, R. F. Chen, B. Guo, T. Hashimoto, Y. Togano, S. Hayakawa, T. Teranishi *et al.*, Phys. Rev. C **88**, 012801 (2013).

[49] H. S. Jung, C. S. Lee, Y. K. Kwon, J. Y. Moon, J. H. Lee, C. C. Yun, M. J. Kim, T. Hashimoto, H. Yamaguchi, D. Kahl, S. Kubono, Y. Wakabayashi, Y. Togano, S. Choi, Y. H. Kim, Y. K. Kim, J. S. Park, E. J. Kim, C.-B. Moon, T. Teranishi *et al.*, Phys. Rev. C **90**, 035805 (2014).

[50] H. Yamaguchi, Y. Wakabayashi, G. Amadio, S. Hayakawa, H. Fujikawa, S. Kubono, J. J. He, A. Kim, and D. N. Binh, Nucl. Instrum. Methods Phys. Res. A **589**, 150 (2008).

[51] H. Kumagai, A. Ozawa, N. Fukuda, K. Sümmerer, and I. Tanihata, Nucl. Instrum. Methods Phys. Res. A **470**, 562 (2001).

[52] D. Kahl, Ph.D. thesis, The University of Tokyo, 2015.

[53] W. J. Jordan, J. V. Maher, and J. C. Peng, Phys. Lett. B **87**, 38 (1979).

[54] S. Hayakawa, S. Kubono, D. Kahl, H. Yamaguchi, D. N. Binh, T. Hashimoto, Y. Wakabayashi, J. J. He, N. Iwasa, S. Kato, T. Komatsubara, Y. K. Kwon, and T. Teranishi, Phys. Rev. C **93**, 065802 (2016).

[55] A. M. Lane and R. G. Thomas, Rev. Mod. Phys. **30**, 257 (1958).

[56] N. M. Larson, *Updated User's Guide for* SAMMY: *Multilevel R-Matrix Fits to Neutron Data Using Bayes' Equations*, Technical

Report No. ORNL/TM-9179/R8, ENDF-364/R2, Oak Ridge National Laboratory, 2008.

[57] C. Rolfs and W. S. Rodney, *Cauldrons in the Cosmos* (the University of Chicago Press, Chicago, 1988).

[58] D. N. Binh, Ph.D. thesis, The University of Tokyo, 2010.

[59] S. Kubono, Z. Phys. A **349**, 237 (1994).

[60] S. Kubono, D. N. Binh, S. Hayakawa, H. Hashimoto, D. Kahl, Y. Wakabayashi, H. Yamaguchi, T. Teranishi, N. Iwasa, T. Komatsubara, S. Kato, and L. H. Khiem, Nucl. Phys. A **834**, 647 (2010).

[61] A. Aprahamian, K. Langanke, and M. Wiescher, Prog. Part. Nucl. Phys. **54**, 535 (2005).

[62] G. V. Rogachev, V. Z. Goldberg, T. Lönnroth, W. H. Trzaska, S. A. Fayans, K.-M. Källman, J. J. Kolata, M. Mutterer, M. V. Rozhkov, and B. B. Skorodumov, Phys. Rev. C **64**, 051302 (2001).

[63] M. Dufour and P. Descouvemont, Nucl. Phys. A **738**, 447 (2004).

[64] K. Setoodehnia, A. A. Chen, D. Kahl, T. Komatsubara, J. José, R. Longland, Y. Abe, D. N. Binh, J. Chen, S. Cherubini, J. A. Clark, C. M. Deibel, S. Fukuoka, T. Hashimoto, T. Hayakawa, J. Hendriks, Y. Ishibashi, Y. Ito, S. Kubono, W. N. Lennard *et al.*, Phys. Rev. C **87**, 065801 (2013).

[65] A. Matic, A. M. van den Berg, M. N. Harakeh, H. J. Wörtche, G. P. A. Berg, M. Couder, J. L. Fisker, J. Görres, P. LeBlanc, S. O'Brien, M. Wiescher, K. Fujita, K. Hatanaka, Y. Sakemi, Y. Shimizu, Y. Tameshige, A. Tamii, M. Yosoi, T. Adachi, Y. Fujita *et al.*, Phys. Rev. C **80**, 055804 (2009).

[66] A. Matic, A. M. van den Berg, M. N. Harakeh, H. J. Wörtche, M. Beard, G. P. A. Berg, J. Görres, P. LeBlanc, S. O'Brien, M. Wiescher, K. Fujita, K. Hatanaka, Y. Sakemi, Y. Shimizu, Y. Tameshige, A. Tamii, M. Yosoi, T. Adachi, Y. Fujita, Y. Shimbara *et al.*, Phys. Rev. C **84**, 025801 (2011).

[67] T. Rauscher and F.-K. Thielemann, Atom. Data Nucl. Data Tables **79**, 47 (2001), http://nucastro.org/websmoker.html

[68] P. M. Endt, Nucl. Phys. A **521**, 1 (1990).

[69] P. Mohr, Eur. Phys. J. A **51**, 56 (2015).

[70] S. Almaraz-Calderon, P. F. Bertone, M. Alcorta, M. Albers, C. M. Deibel, C. R. Hoffman, C. L. Jiang, S. T. Marley, K. E. Rehm, and C. Ugalde, Phys. Rev. Lett. **112**, 152701 (2014).

[71] J. R. Tomlinson, J. Fallis, A. M. Laird, S. P. Fox, C. Akers, M. Alcorta, M. A. Bentley, G. Christian, B. Davids, T. Davinson, B. R. Fulton, N. Galinski, A. Rojas, C. Ruiz, N. de Séréville, M. Shen, and A. C. Shotter, Phys. Rev. Lett. **115**, 052702 (2015).

[72] S. Almaraz-Calderon, P. F. Bertone, M. Alcorta, M. Albers, C. M. Deibel, C. R. Hoffman, C. L. Jiang, S. T. Marley, K. E. Rehm, and C. Ugalde, Phys. Rev. Lett. **115**, 179901(E) (2015).

[73] A. M. Howard, M. Munch, H. O. U. Fynbo, O. S. Kirsebom, K. L. Laursen, C. A. Diget, and N. J. Hubbard, Phys. Rev. Lett. **115**, 052701 (2015).

[74] T. Anderson, M. Skulski, A. Clark, A. Nelson, K. Ostdiek, P. Collon, G. Chmiel, T. Woodruff, and M. Caffee, Phys. Rev. C **96**, 015803 (2017).